Vacuum 239 (2025) 114449

Contents lists available at ScienceDirect

Vacuum

journal homepage: www.elsevier.com/locate/vacuum

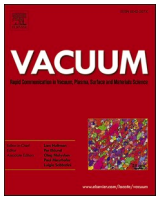

Probing the impact of rough vacuum on the early-stage evolution of ns laser-produced tungsten plasma

M.S. Amogh [a,b], Sebin Sebastian Xavier [a], Cyril Benny [a], Pranitha Sankar [a], Nancy Verma [a,1], Reji Philip [a,*]

[a] Raman Research Institute, C.V Raman Avenue, Sadashivanagar, Bangalore, 560080, India
[b] School of Pure and Applied Physics, Mahatma Gandhi University, Kottayam, 686560, India

ARTICLE INFO

Handling Editor: Prof. L.G. Hultman

Keywords:
Optical emission spectroscopy (OES)
Tungsten LPP
Laser interferometry
Shadowgraphy
Image analysis

ABSTRACT

A detailed time-resolved analysis of laser-produced plasmas (LPPs) is essential for understanding the effects of ambient gas on plasma characteristics. In this work, a nanosecond pulsed laser (1064 nm, 7 ns) generates LPPs from a tungsten (W) target, which is comprehensively analyzed using optical emission spectroscopy, laser plasma interferometry, shadowgraphy, and imaging. Measurements reveal that varying the ambient pressure in the 1.33 $\times$ 10^3 Pa - 5.33 $\times$ 10^4 Pa range significantly affects the plasma temperature, number density and plume morphology. Spectral analysis reveals a strong correlation between number densities obtained from Stark broadening measurements of the H-alpha and W I lines. The interferometric method enables the study of plasma plume morphology and retrieval of number densities even in the presence of strong continuum emission. Density maps obtained from interferometry show inhomogeneities. Shadowgraphy images show the expansion of shockwaves at different pressures, and they also reveal that the transition of plasma from non-collective to collective behavior occurs around 1 $\times$ 10^4 Pa. Despite inhomogeneities, plasma remains in Local Thermodynamic Equilibrium during the observed time window of up to 1 μs. Due to well-established Stark parameters and strong linear correlation with the W I line, the H-alpha line provides a more straightforward estimation of number densities in tungsten LPPs.

1. Introduction

Laser-produced plasmas (LPPs) display complex and dynamic characteristics encompassing a wide range of parameters such as temperature, number density, charge states and charged particle kinetics. These parameters depend on many factors such as the irradiation conditions, target geometries and the background medium [1,2]. Multiple techniques are available for determining the plasma parameters such as temperature and number density, including Langmuir probe, laser interferometry, Thomson scattering, and Optical emission spectroscopy (OES) [2–5]. The OES of LPPs, commonly referred to as Laser Induced Breakdown Spectroscopy (LIBS), is an excellent technique for providing rapid, in-situ, and non-destructive quantitative analysis of materials [5–7]. LIBS has widespread applications in defence, archaeology, biology, robotic planetary exploration and various industries like nuclear, solar, mining and waste management [8–13]. The key advantages of LIBS over other techniques are the non-requirement of sample pre-processing, remote sensing capability and the analysis speed. The spectra and the continuum emission from the LPPs depend on the temperature, electron number density and the number densities of the constituent atoms and ions. Therefore, a comprehensive LPP characterization is important in improving LIBS accuracy.

It is important to recognize that LPPs, and hence LIBS, is inherently complex due to the many parameters governing its properties, including laser parameters such as energy, pulse duration and beam spot size, and ambient gas parameters such as pressure and type. The surrounding gas's type and pressure significantly impact the properties of LPPs, resulting in its confinement, splitting, sharpening, energy transfer to the background and shockwave generation. Plasma parameter gradients have been observed in the presence of background gases and air [14–16]. Plume splitting and sharpening are observed in laser-produced aluminium plasmas, where the plume front is spherical at early times. As it expands, the plume front gets sharpened. It splits into fast and slow components at a pressure range where the transition of collisional to

* Corresponding author
E-mail address: reji@rri.res.in (R. Philip).
[1] Present address: Department of Physics, Allahabad Degree College, University of Allahabad, 211002, India.

https://doi.org/10.1016/j.vacuum.2025.114449
Received 19 February 2025; Received in revised form 5 May 2025; Accepted 23 May 2025
Available online 26 May 2025
0042-207X/© 2025 Published by Elsevier Ltd.

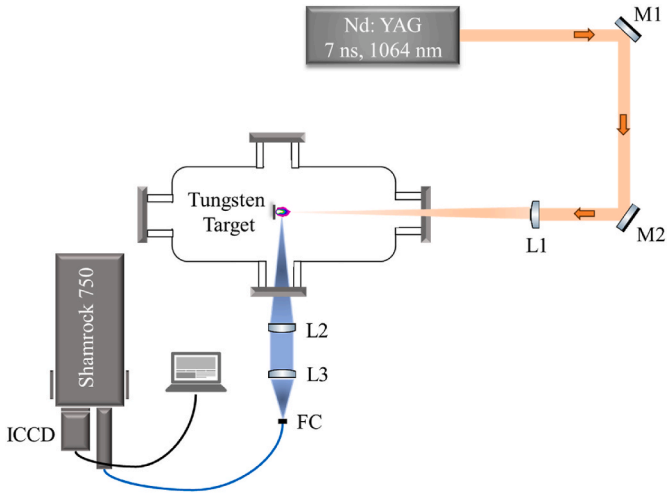

Fig. 1. Schematic of the experimental setup used for Optical Emission Spectroscopy measurements of laser-produced tungsten plasma. M: Mirror, L: Lens, FC: Fiber coupler.

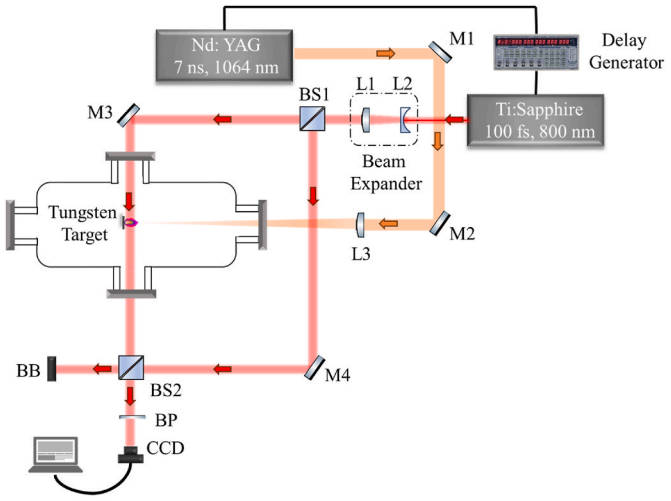

Fig. 2. Geometry of the interferometry setup used for measurements of laser-produced tungsten plasma. M: Mirror, L: Lens, BS: Beam-splitter, BP: Band-pass filter, BB: Beam block.

collisionless interaction of the plume with the background gas happens [17]. For lower background pressures, the interaction of the ablated vapour with the surrounding gas occurs through diffusion, and for higher pressures, collective processes dominate and can lead to shock-wave propagation. The collective and non-collective behaviour of plasma is dynamic under the influence of background pressure. It is susceptible to the local number density and ambient gas species and thus can depend on the laser fluence and the target material [14,18]. One way to alleviate the complexity of the dynamic laser-produced plasmas is to consider them as homogenous and assume that they follow Local Thermodynamic Equilibrium (LTE) conditions [5,19]. However, care should be taken for the transient and inhomogeneous nature of the plasma while assessing LTE conditions, where the plasma's relaxation processes and diffusion length of atoms/ions play a critical role [20].

In most tokamaks, the primary choice of material for plasma facing component (PFC) is tungsten, which is used as a first material wall because of its low retention of fusion fuel compared to other elements such as C. It is also a good material for divertor in ITER due to its high melting point, sputtering yield and low tritium retention [21,22]. Regular diagnostic assessments of the reactor wall material are crucial for ensuring the safety of ITER-like tokamaks. LIBS has been shown as an ideal candidate for the real-time, online diagnostics of impurity and fuel retention on the first wall and divertor tiles in tokamaks. LIBS has been used for the quantitative study of retention of fusion fuel on tungsten substrates [23,24]. A comprehensive study of LPPs from tungsten targets is essential for improving PFC diagnostics. Further, in additive manufacturing with tungsten, understanding plasma dynamics in rough vacuum conditions can be beneficial for quantifying the alloying elements, that can help mitigate cracking [25]. Understanding laser plasma behavior under rough vacuum conditions is crucial for quality control in additive manufacturing, as LIBS enables precise elemental analysis [26]. These processes are carried out in rough vacuum conditions which can be attained by a single environment friendly diaphragm pump or oil free scroll pump as opposed to complex multi-stage setups. Rough vacuum levels are also highly beneficial for material processing, micro-machining, and laser-based manufacturing [27]. Moreover, laser produced tungsten and tungsten alloy plasmas have been studied for qualitative and quantitative studies including the dependence on laser fluence, spot size, different ablation geometries and microstructural properties [21,28–33]. The effect of pressure on laser-produced tungsten plasma in the range 10^{-3} Pa–10^{5} Pa using OES and imaging were used to optimize the LIBS in a coaxial optical geometry [34]. The LTE conditions of tungsten plasma using time resolved OES have been verified at atmospheric pressure at various laser fluences, where the validity of LTE in tungsten plasma is discussed with plasma relaxation processes and diffusion length [35]. In another previous study, the effect of pressure up to atmospheric on laser-produced tungsten plasma in large pressure intervals and longer gate-delays have been investigated [34].

Here we use complementary approaches for a better understanding of the evolution of the plasma parameters, spatial electron density distribution, inhomogeneities in the plasma, and validity of LTE for the early plume expansion time window (up to 1 μs), at ambient pressures $>1.33 \times 10^{3}$ Pa where collective behaviour is observed. Within this pressure range, combining spectroscopic methods with techniques like laser interferometry and shadowgraphy provides valuable insights into collective behavior and its impact on plasma evolution and gradients during the first few hundred nanoseconds after formation.

2. Experimental setup

2.1. Optical emission spectroscopy and imaging

1064 nm pulses of energy 35 mJ with a pulse width (FWHM) of 7 ns, obtained from a Q-Switched Nd: YAG laser (Quanta Ray, Spectra-Physics) with a repetition rate of 10 Hz were used for generating plasma from the tungsten surface (Fig. 1). The input energy is controlled by using a combination of half-wave plate and polarizing beam splitter. The beam is focused on to the tungsten target (99.99 % pure) which is mounted on a movable stage placed inside the vacuum chamber using a 40 cm plano-convex lens. For imaging, laser-produced plasma emission is guided onto an intensified charge-coupled device (ICCD, Andor i-star 334 T) using a combination of two plano-convex lenses of focal lengths 25 cm and 50 cm respectively. The time-resolved emission spectra are recorded using the same ICCD employing a 0.75 m Czerny-Turner spectrometer (Shamrock 750) having a 1200 grooves/mm grating. The input slit was kept at 30 μm width. The ambient gas in this study is air, with humidity maintained at 70 % at 20^{0} C. The vacuum chamber is connected to a dry pump (DBP 050–4, Pfeiffer Vacuum) to reduce the pressure and a leak valve to inject air to the vacuum system. A pressure gauge (TPR 200, Pfeiffer Vacuum) monitors the pressure.

2.2. Interferometry and shadowgraphy

Interferometry: A Mach-Zehnder interferometer (Fig. 2) was set up to measure the electron number density of the laser-produced tungsten plasma [36]. 100 fs laser pulses of 800 nm wavelength (TSA:

Table 1
Spectral lines used for temperature and number density calculations.

Wavelength (nm)	Ionization	E_j (eV)	E_i (eV)	A_{ij} (s^{-1})10^7
424.14	W I	4.839134	1.916797	5.35
424.44	W I	3.691424	0.771099	1.52
426.93	W I	3.269126	0.365913	1.52
427.54	W I	5.145274	2.246202	6.5
434.81	W II	4.483932	1.633285	1.01

Spectra-Physics) and beam diameter ~8 mm are used to produce the interferograms. The beam was expanded ~2 times using a Galilean telescope beam expander configuration consisting of two lenses of focal lengths −25 cm and 50 cm respectively. The time-resolved interferograms are captured using a CCD camera (Thorlabs DCU224C). A single plano-convex lens of 25 cm was used to direct the interferograms to the CCD. A narrow bandpass filter (800 nm) was used to reduce the coupling of the intense plasma continuum emission to the CCD. A digital delay generator (Stanford Research Systems DG645) was used to vary the delay between the lasers pulses. The noise and high-frequency components in the interferograms are filtered out using a Gaussian filter in the frequency domain.

Shadowgraphy: The probe beam was expanded to 2 cm diameter for focused shadowgraphy. Two plano-convex lenses (25 cm and 10 cm) were used to collect the shadowgrams onto the CCD. A digital delay generator (Stanford Research Systems DG645) was used to vary the delay between the laser pulses for taking measurement.

3. Results and discussion

3.1. Determination of temperature and number density from spectra

The temperature of the tungsten plasma was obtained by the Boltzmann plot method. For a plasma in Local Thermodynamic equilibrium (LTE), the spectral line intensity of an electronic transition between the upper (j) and lower (i) levels is related to the upper energy state E_j and temperature T by the equation,

$$\ln\left(\frac{I_{ij}\lambda_{ij}}{g_j A_{ij}}\right) = \frac{1}{k_B T}E_j + \ln\left(\frac{hcn}{4\pi \mathrm{U(T)}}\right) \quad (1)$$

where λ_{ij} is the wavelength corresponding to the transition from j to i, g_j is the statistical weight of the upper level, A_{ij} is the transition probability, T is the temperature, n is the number density of the ionization stage, and U(T) is the partition function of the element under consideration. The temperature is obtained from the slope of the Boltzmann plot utilizing several transitions. The electron number density n_e is obtained from the Saha-Boltzmann method given by the equation,

$$n_e = \frac{I^z g^{z+1} A^{z+1} \lambda^z}{I^{z+1} g^z A^z \lambda^{z+1}} \left(\frac{2\pi m_e k_B T}{h^2}\right)^{\frac{3}{2}} 2 \times \exp\left[-\left(\frac{E^{z+1} - E^z + E_{IP}}{k_B T}\right)\right] \quad (2)$$

where z and z+1 correspond to the degree of ionization. E_{IP} is the ionization potential [37].

The lowering of the ionization potential due to plasma interaction is neglected in the calculation of the electron number densities. The spectral lines used for the temperature and number density calculations are shown in Table 1. It is to be mentioned that both methods are used under the assumption that the plasma is in LTE during the window of observation (gate delays of 0.1–1.0 μs, and gate-width of 100 ns). The minimum n_e value that warrants the plasma to be in LTE is given by the McWhirter criterion,

$$n_e(cm^{-3}) > 1.6 \times 10^{12} T^{\frac{1}{2}} (\Delta E_{ij})^3 \quad (3)$$

where T and ΔE_{ij} are in K and eV units respectively. Based on the first resonant line of W I ($\Delta E_{ij} = 3.22$ eV), the lower bound of number densities obtained from Equation (3) for the temperature range in our study is 5.46–6.71 × 10^{15} cm^{-3} for all ambient pressures. While this condition is necessary, it is not sufficient to confirm LTE. A more reliable way to assess LTE includes a comparison of number densities obtained from different methods such as the McWhirter expression, Saha equation and Stark broadening of suitable lines [20].

To verify the number densities obtained, we choose the Stark broadening method, which is successfully used to estimate n_e even for plasmas which have a gradient in plasma parameters. The electron number density is related to the FWHM of the stark broadened line according to the following equation,

$$n_e = \frac{\Delta FWHM}{w_s}(10^{17}\ cm^{-3}) \quad (4)$$

The stark broadening parameter w_s of the W I line (429.4 nm) is used to find n_e [38,39]. We also utilize the Stark broadening of the Hα line in our calculations [36]. The electron density can be calculated from the FWHM of the Stark-broadened H_α line at 656.28 nm because Hydrogen Balmer lines are sensitive to the micro-field induced by charged particles in the plasma [38,40,41,42]:

$$n_e = 8.02 \times 10^{12} \left[\frac{\Delta \lambda_{\frac{1}{2}}}{\alpha_{\frac{1}{2}}}\right]^{\frac{3}{2}} \quad (5)$$

where $\alpha_{1/2}$ is a coefficient which is weakly dependent on the temperature and pressure through ion-ion correlation, Debye-shielding correction, and impact broadening. $\Delta\lambda_{1/2}$ is the FWHM of the H_α line fitted with the Lorentzian profile. The $\alpha_{1/2}$ coefficients are obtained from

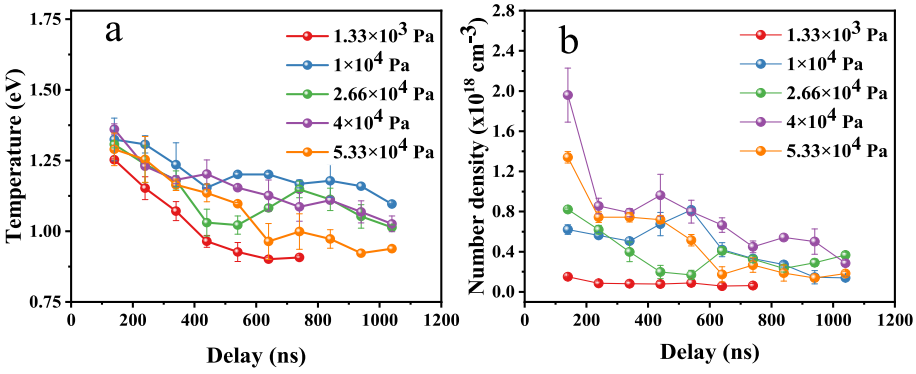

Fig. 3. Temporal evolution of the temperature (a) and number density (b) of laser produced tungsten plasma at different pressures ranging from 1.33 × 10^3 Pa to 5.33 × 10^4 Pa. The emission spectra are collected 0.5 mm away from the target surface with gate interval and gate width of 100 ns each.

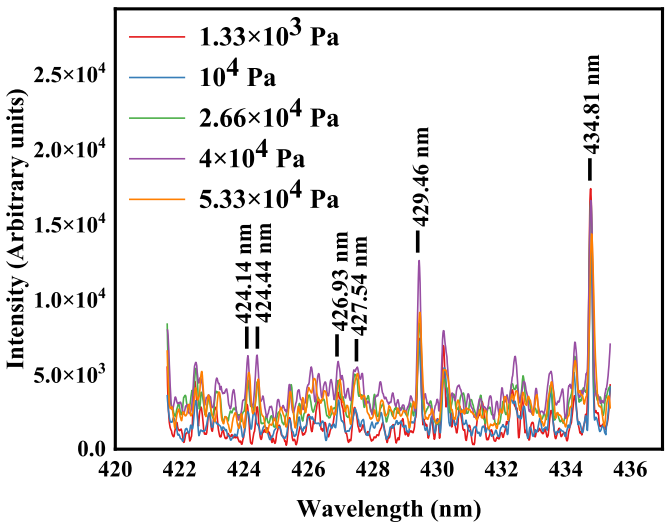

Fig. 4. Time resolved optical emission spectra of Laser produced tungsten plasma at different ambient pressures from 1.33 × 10^3 Pa to 5.33 × 10^4 Pa at delay 240 ns.

Ref. [43].

Fig. 3(a) shows the temperature calculated from the W I lines given in Table 1, and Fig. 3(b) shows the evolution of the number densities calculated from the W II line (434.81 nm) and W I line (427.54 nm). For the aforementioned slit width the instrumental broadening was found to be approximately 0.034 nm by using a narrow bandwidth HeNe laser. Fig. 4 shows the optical emission spectra of laser produced tungsten plasma at pressures ranging from 1.33 × 10^3 Pa to 5.33 × 10^4 Pa. At 1.33 × 10^3 Pa the decrease in n_e and temperature are gradual, which may indicate minimal influence from the background air (See Fig. 3). The higher pressures of 1 × 10^4 - 5.33 × 10^4 Pa exhibit a distinctive pattern where T and n_e show spikes within the observation window of 1 μs, which could be due to the shockwave formation resulting from the interaction of plasma with the ambient air. The rapid reduction of n_e for the pressures 4 × 10^4 Pa and 5.33 × 10^4 Pa in the initial delays, compared to lower pressures, is possibly due to the collision of the plasma with the background air and consequent energy transfer. This decrease is more prominent at 4 × 10^4 Pa and 5.33 × 10^4 Pa, suggesting considerable energy transfer to the background [44,45]. The highest number density values were observed at 4 × 10^4 Pa and 5.33 × 10^4 Pa with a 140 ns delay, potentially indicating enhanced laser-matter coupling during the initial stages of plasma formation at these pressures, along with the influence of pressure confinement. Therefore, even though laser-matter coupling and ambient gas confinement are strong at these pressures, collisions with the background gas cause a rapid decline in n_e.

Similar to the Saha-Boltzmann method, the number densities obtained from the Stark broadening of the W I and H_α lines also show a decreasing trend (Fig. 5). The corresponding Lorentzian fits are also displayed. The similarity between electron densities calculated from the WI line and Hα lines is high as seen in Fig. 6(a), giving correlation values (r) greater than 0.9. Although a robust linear relationship exists between the two measured number densities from the stark broadening of H_α and W I, these number densities are generally less compared to those obtained from the Saha-Boltzmann equation. Higher estimates of electron density derived from the Saha-Boltzmann equation have been observed for Al and Mg emission lines, making it particularly suitable for temporal profiling rather than for specific conditions [46]. The observed differences in electron density between the methods may be attributed to plasma inhomogeneity, where the populations of W I, W II, and H atoms exhibit spatial separation [47,48]. This separation can effectively diminish Stark broadening along the line of sight. However, as discussed above, the highest number densities are observed at 4 × 10^4 Pa and 5.33 × 10^4 Pa pressures. The strong correlation between W I and H_α line methods makes measuring Stark broadening of spectral lines a relatively

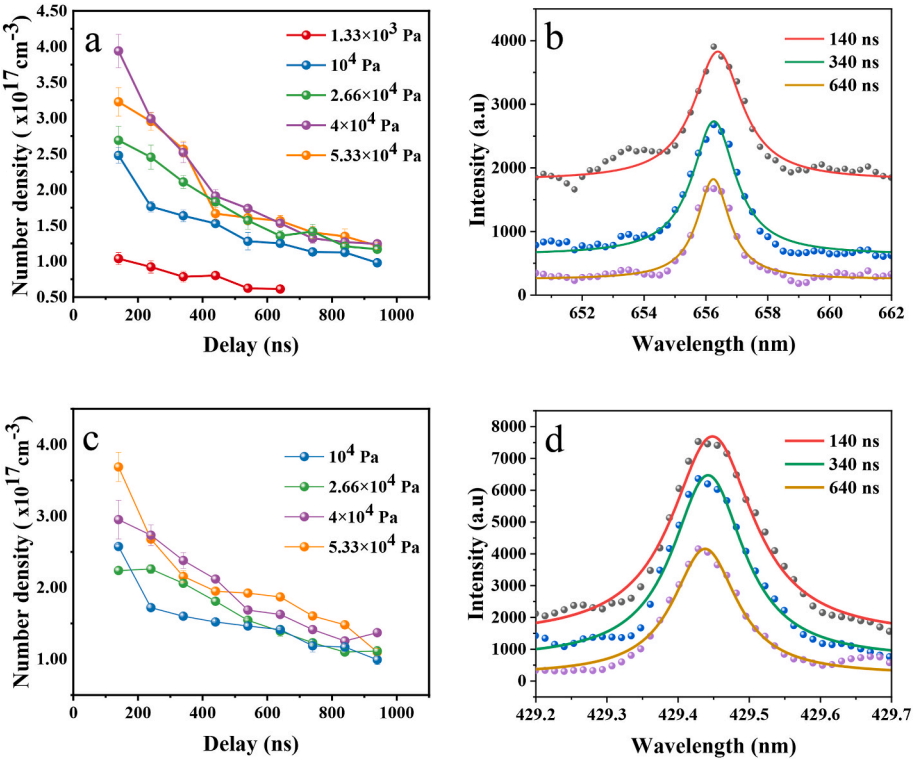

Fig. 5. (a) Number densities from H_α line (b) The Lorentzian fits to the line profile at 1 × 10^4 Pa for the delays 140 ns, 340 ns and 640 ns.(c) Number densities from W I line 429.4 nm nm with w_s = 0.0513 nm [38]. (d) The Lorentzian fits to the W I line at 1 × 10^4 Pa.

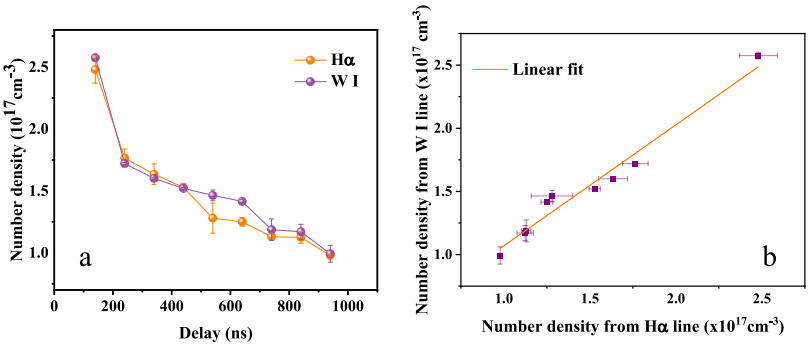

Fig. 6. (a) Number densities obtained from emission spectra using the Saha-Boltzmann method using W I and W II lines of tungsten and the H_α line. Ambient pressure is 1×10^4 Pa. (b) Scatter plot of number densities obtained from tungsten spectra and H_α line, where each point is for different time delays at 1×10^4 Pa. Pearson's r value is 0.98 showing a strong correlation between the calculated number densities.

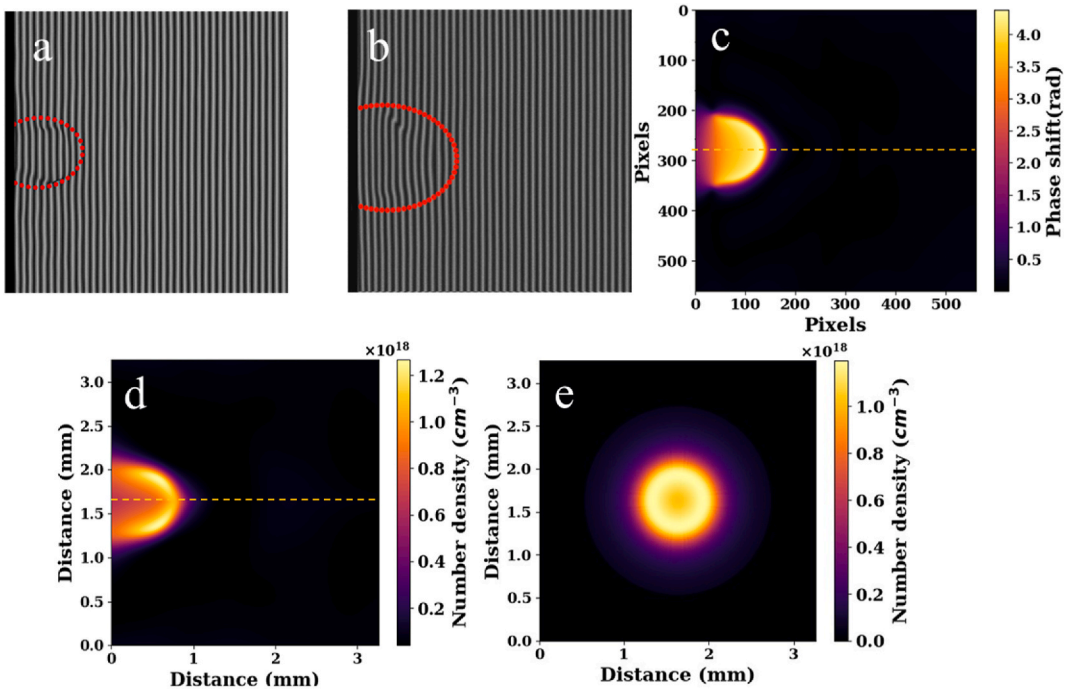

Fig. 7. (a) Interferogram at 80 ns, (b) interferogram at 240 ns showing negative fringe shift, (c) phase map at 80 ns, (d) number densities at 80 ns delay and 1×10^4 Pa. The dotted line represents the symmetry axis of the plume. (e) The radial density distribution at an axial distance of ~0.3 mm from the target representing the inhomogeneity in the plasma.

more straightforward method for determining n_e of Laser produced tungsten plasma [38].

3.2. Determination of number density from interferometry

We use femtosecond laser plasma interferometry [49] to probe electron number density evolution and spatial distribution where the continuum emission is present. The electromagnetic waves in one of the interferometer arms acquire a phase due to the optically thin plasma resulting in a distortion of the interferogram. From the interferograms, the interferometric phase wrapped in the range $(-\pi, \pi)$ can be unwrapped to obtain the smooth phase field [50]. The phase shift $\Delta\phi$ is then obtained by taking the difference of the unwrapped interferogram in the presence and absence of laser-produced plasma. The electron density is related to the phase shift by

$$\Delta\varphi = \frac{\pi}{n_c}\int n_e dr \tag{6}$$

Where $n_c = 1.11 \times 10^{21}/\lambda_{nm}^2$ cm^{-3} is the critical density which is 1.74×10^{21} cm^{-3} for our probe beam [51] and λ_{nm} is the probe beam wavelength in μm. Under the assumption that the plume has an axial symmetry, the spatially resolved number densities are retrieved through an Abel inversion [52]. By assuming that radial projection data are taken at equally spaced radial positions Δr, the Abel integral can be solved by a deconvolution operator D_{ij} acting on the Line-of-Sight integrated projection ϕ(r) [53],

$$F(r_i) = \frac{1}{\Delta r}\sum_{j=0}^{\infty} D_{ij}\,\varphi(r_j) \tag{7}$$

Using the linear operator method, we eliminate the need to calculate derivatives of the phase in the Abel integral, as well as avoid the divergence of values along the symmetric axis [50]. The phase retrieval is done under the assumption that the major contributor to the phase shifts of the interferogram are the free electrons (positive fringe shift) and the total refractive index is less than unity. Fig. 7(a) and (b) show

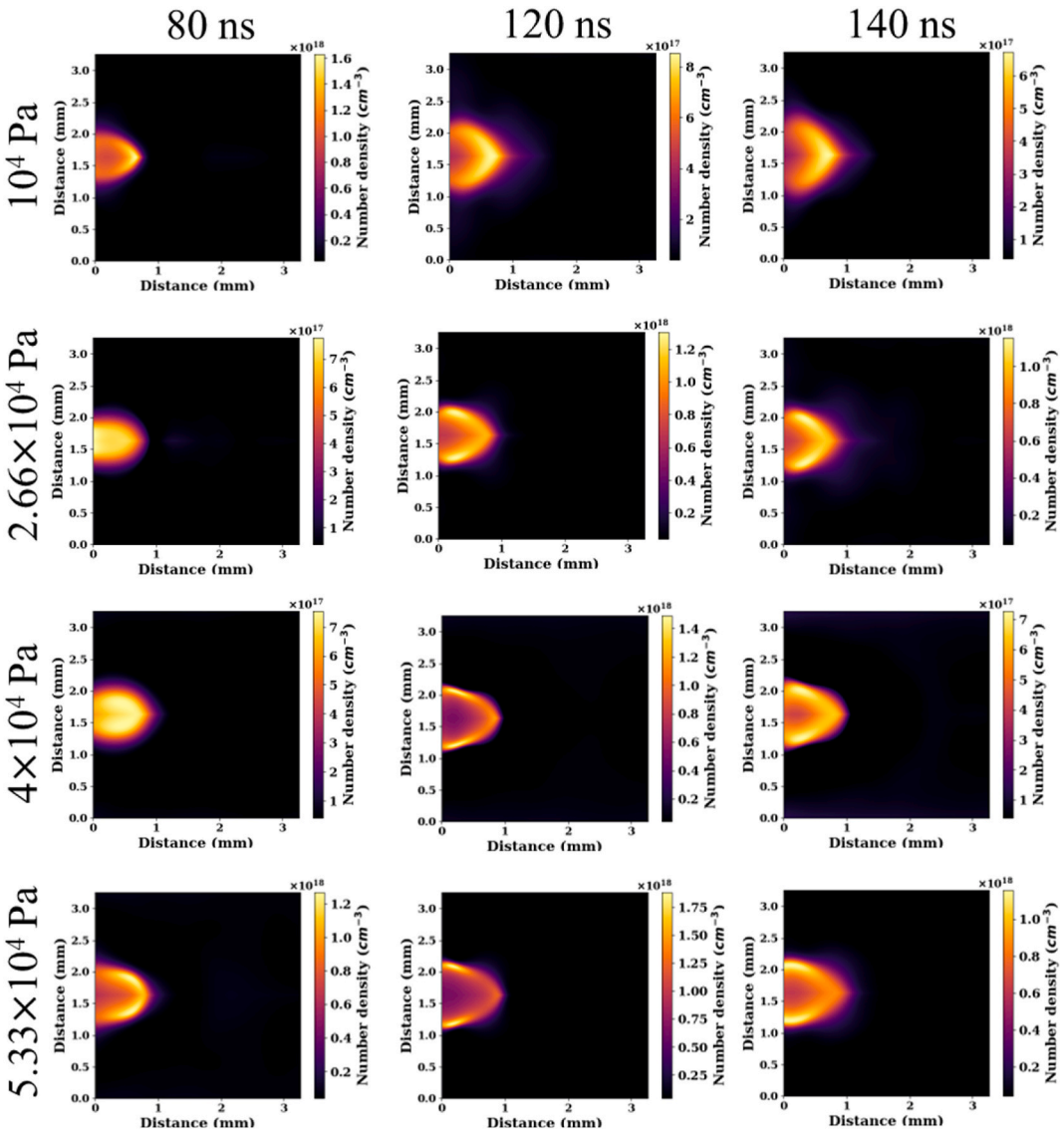

Fig. 8. Number densities obtained for time delays 80 ns, 120 ns and 140 ns when continuum emission is present. The inhomogeneities in the plume are visible. The plume edge becomes sharper as the delay is increased for 4 × 10^4 Pa and 5.33 × 10^4 Pa pressures.

interferograms taken at 80 ns and 240 ns delay, respectively, while Fig. 7 (c)-7(d) present the retrieved phase map and electron density distribution at 80 ns, and Fig. 7(e) illustrates the radial electron density distribution at an axial distance of ~0.3 mm from the target at 80 ns. All images were taken at 1 × 10^4 Pa pressure. In the time scale 80 ns – 140 ns the phase shift and the electron number density show inhomogeneity where the density closer to the target is lower than the periphery (See Figs. 7 and 8). The maximum number density reaches ~1.5 × 10^{18} cm^{-3} (delays of 80 ns and 120 ns). It is also observed that, starting at 4 × 10^4 Pa, the plasma gets transitioned from a spherical to an axially elongated form (plume sharpening) with increasing delay for high pressures. Many experiments have demonstrated that LIP expansion dynamics is highly dependent on both background gas pressure and composition. Previous studies, particularly in applications such as pulsed laser deposition (PLD), have shown that LIP dynamics transitions from nearly free-plume expansion at very low pressures to plume splitting (the formation of multiple components) and plume sharpening at higher pressures [54]. This behavior is consistent with our observations, where plume sharpening becomes prominent as the ambient gas pressure is increased. In contrast, at 1 × 10^4 Pa and 2.66 × 10^4 Pa, the effect is reversed for the initial delays. Throughout the expansion, the maximum number density is observed at the distance of a few millimeters from the target. The deviation of plasma shape from spherical can be attributed to the anisotropy in the axial and radial expansions due to the forward-directed nature of plume evaporation [55]. The same axial pull towards the laser direction could also be the reason for the maximum number density to shift away from the target surface. The average values of the electron number densities from the interferograms at 140 ns for all studied pressures are within the range 3.5 × 10^{17} cm^{-3} to 5.7 × 10^{17} cm^{-3}. These densities are in the range of densities obtained from W I and H_α lines and can be correlated to the spectral measurements [3,51].

We notice that at later times of plasma evolution, the plume edges contribute to a negative fringe shift, where fringes bend towards the target side. Since the fringe shift is positive for earlier times of plasma evolution (<140 ns), where free electron density is high, the negative fringe shift after 140 ns (Ref Fig. 7 (b)) could be due to bound electron contribution to the total phase shift. The influence of the bound electrons on the refractive index at photon wavelengths located orders of magnitude further from the line centers and resonance lines has been suggested [56,57]. Thus, although there are no resonance or near-ground level tungsten lines within the 12 nm spectral bandwidth of the probe pulse centered at 800 nm, the contribution of bound electrons

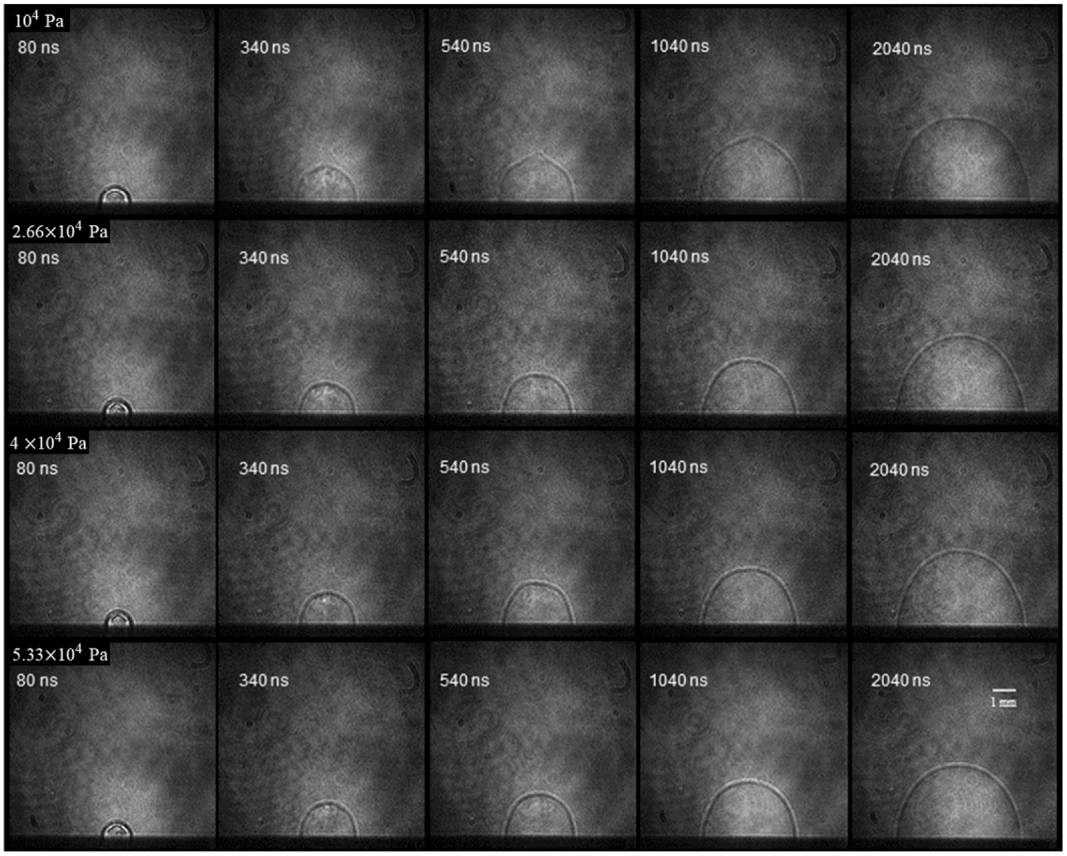

Fig. 9. Shadowgraphs showing shockwave formation from time delay 80 ns to 2 μs at different ambient pressures.

remains evident, as resonance lines can influence the refractive index at photon energies significantly beyond their linewidth resulting in the fringe reversal [58,59]. This is an indication that the bound electron contribution in the plume edge could be either from the WI or W II transitions since the higher charge states are found in the hot region of the plasma [60].

As it is evident that the laser-produced tungsten plasma is inhomogeneous and transient, two additional criteria should be met for the plasma to be in LTE other than McWhirter. These are given by the relations [20]:

$$\frac{T(t+\tau_{rel})-T(t)}{T(t)} < < 1 \quad \frac{n_e(t+\tau_{rel})-n_e(t)}{n_e(t)} \ll 1 \tag{8}$$

and

$$\frac{T(x)-T(x+\lambda)}{T(x)} < < 1 \quad \frac{n_e(x)-n_e(x+\lambda)}{n_e(x)} < < 1 \tag{9}$$

where τ_{rel} is the time needed to establish excitation and ionization equilibria, and λ is the diffusion length during the time τ_{rel} which is given by

$$\tau_{rel} \approx \frac{6.3\times10^4}{n_e f_{12} < \bar{g} >} \Delta E_{ij} (kT)^{\frac{1}{2}} exp\left(\frac{\Delta E_{ij}}{kT}\right) \tag{10}$$

where f_{12} is the transition strength and g is the Gaunt factor [30]. For $\Delta E_{21} = 3.22$ eV, τ_{rel} is in the range of $\sim10^{-9}$ s for the present study, ensuring that thermodynamic parameters vary sufficiently slowly so that electrons and atoms have enough time to reach equilibrium. An inhomogeneous plasma's equilibrium condition is met when the plasma plume diameter is at least 10 times larger than its diffusion length λ,

$$\lambda \approx 1.4\times10^{12} \frac{(kT)^{\frac{3}{4}}}{n_e} \left(\frac{\Delta E}{M_A f_{12} < \bar{g} >}\right) exp\left(\frac{\Delta E}{2kT}\right) \tag{11}$$

where M_A is the relative mass of species considered, λ is$\sim10^{-5}$ cm, and the plume diameter is $\sim10^{-1}$ cm, verifying LTE [20].

3.3. Shadowgraphy and image analysis

A hot and dense plasma that expands rapidly in an ambient medium compresses the air around it and generates a shock wave. Focused shadowgraphy is used to probe the evolution of the shockwaves formed during the ablation of tungsten in the pressure range 1×10^4 Pa to 5.33×10^4 Pa.

The obtained shockwaves are shown in Fig. 9. The shockwave follows the same shape as the plasma plume in the early stages of evolution leading to shock edge elongation in the expansion direction due to the plasma shielding of laser energy [61,62]. Due to this the shock radius is calculated along the target surface because the plume and hence the shockwave elongation due to absorption of the laser energy happens predominantly in the direction of the laser pulse. For strong shocks with Mach number M > 7 the propagation can be modelled by a point explosion for a spherical wavefront by Taylor-Sedov theory [35,63,64],

$$R = \left(\frac{E}{K\rho}\right)^{1/5} t^{2/5} \tag{12}$$

where R, E, v_s, and ρ are the radius of the shockwave, adsorbed energy, speed of sound and unperturbed density, respectively. K is a quantity that depends on the specific heat and varies between 0.6 to 0.8. By using the Taylor- Sedov model the blast energy E can be obtained which shows how much energy was spent on the expansion of the shockwave after energy losses due to plasma shielding and the sample's thermal

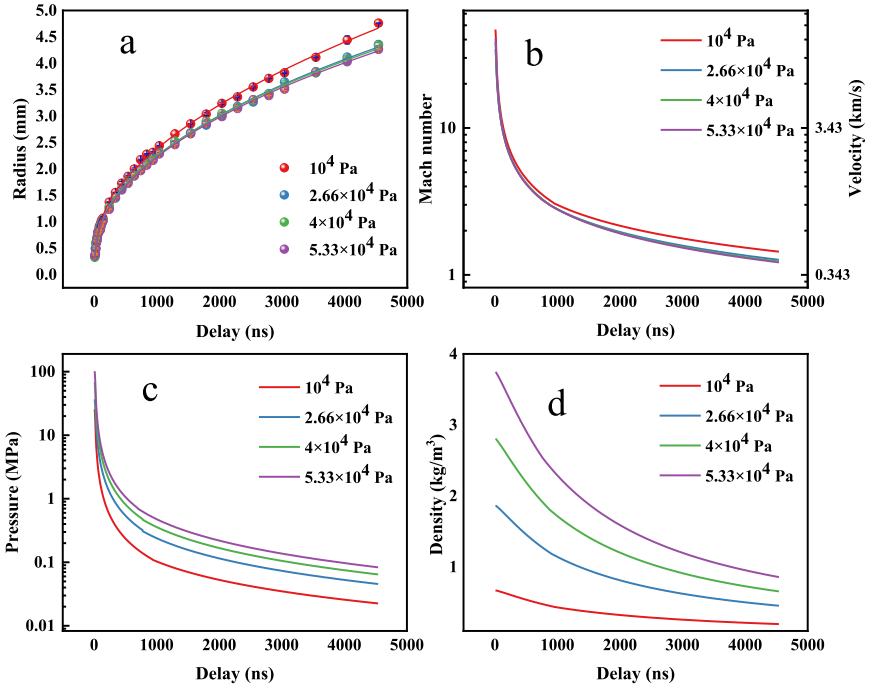

Fig. 10. (a) Radius (b) Velocity (c) Pressure and (d) Density of the shockwave front at pressures 1 × 10^4 Pa to 5.33 × 10^4 Pa.

Table 2
Adsorbed energy E from Taylor-Sedov model and A, t_0 and n obtained from exponential fits. The exponential model is fitted from 240 ns onwards.

Pressure (Pa)	E (mJ)	A	t_0 (ns)	n
1 × 10^4 Pa	8 ± 0.2	1.66 ± 0.3	−147 ± 4.4	0.47 ± 0.01
2.66 × 10^4	17.1 ± 0.03	1.1 ± 0.16	−91.8 ± 3.4	0.45 ± 0.01
4 × 10^4	25.3 ± 0.04	0.957 ± 0.14	−66.9 ± 2.7	0.44 ± 0.009
5.33 × 10^4	32.1 ± 0.05	0.91 ± 0.09	−48.7 ± 2.0	0.43 ± 0.007

conductivity. It has been suggested that the blast wave model may provide an upper estimate of the initial energy [52]. Further, when the shockwave velocity approaches the sound velocity, the exponential in the Taylor- Sedov model deviates from the value (2/5) and tends to be higher [61,65]. Since this model agrees well in the initial stages of shockwave expansion and deviates when the shock becomes of intermediate strength, the expansion for shocks of intermediate strength for all pressures is modelled by a simple exponential fit $R = A\ (t\text{-}t_0)^n$. The factor t_0 is introduced to offset the non-zero initial value of time, and the exponential accounts for the deviation from the Taylor-Sedov model. The shockwave expansion trajectories obtained from the shadowgraphs (Fig. 10) show rapid evolution of the shockwaves at the lower pressure of 1 × 10^4 Pa. The velocities, along with the corresponding shock densities and pressures calculated using the Rankine-Hugoniot relations (see Supplementary Material), are also presented. The shocks are hypersonic for time delays less than ~300 ns. The radius of expansion and velocity at a given time are high for 1 × 10^4 Pa compared to higher pressures. For the pressures 5.33 × 10^4 Pa, 4 × 10^4 Pa and 2.66 × 10^4 Pa the expansion is very similar in terms of radius, but a significant difference is seen in their densities and pressures since the Rankine-Hugoniot relations are very sensitive to the Mach velocity of the shock front. The shockwave pressure and density are the highest for 5.33 × 10^4 Pa with the highest pressure being ~100 MPa.

The fitting parameter E for the Taylor-Sedov model and the parameters A, t_0 and n for the exponential fit are listed in Table 2. As the pressure decreases, the energy deposited E, obtained from the Taylor-Sedov model, gets reduced. This reduction in energy could mean that the pulse energy is being deposited somewhere else other than for shockwave generation, which may point to laser supported detonation (LSD) and plasma shielding at lower pressures. Since the shockwave shape is closely related to the shape of the plume that displaces the ambient gas, plume splitting is evident from the shadowgraph at 1 × 10^4 Pa (around ~ 540 ns). The shockwave front is found to be distorted at this time delay. Notably, this is also the pressure where the E value from the Taylor-Sedov fit drops to the lowest. However, a definitive conclusion on LSD or plasma shielding could not be established, as obtaining E values at lower pressures was hindered by the limited visibility of the shockwaves.

Fast imaging of the plume was done using a gated ICCD. Spectrally integrated images of the plume were taken at different gate delay times (t_d) for pressures from 5.33 × 10^4 Pa – 13.3 Pa. Two sets of images were taken, namely, (a) images taken with 10 ns gate width (t_w), and (b) images with gate width equal to 10 % gate delay (for delays above 500 ns). Those taken with t_w = 10 % t_d are found to contain more information, and hence have been used in the analysis [34]. The position of the plume front can be obtained from the plume images (Fig. 11), which can then be plotted against the delay time (R-t plot, Fig. 12). It can be seen that at lower pressures, the interaction of the plasma with the background gas is minimal, and the plume expands freely. As the pressure increases beyond 1.33 × 10^2 Pa the plasma interacts with the background gas, changing the plume expansion dynamics. At moderately high pressures the background gas interpenetrates the plasma, and at still higher pressures the dynamics of the plasma is entirely determined by the nature and properties of the background gas. Thus, the plasma expands adiabatically at low pressures (~13.3 Pa), where the background gas has minimal influence, resulting in an R-t plot that follows a linear expansion model. The plume front follows the shock wave model for pressures ranging from 1.33 × 10^2 Pa to 1 × 10^4 Pa as background gas confinement effects become significant. For pressures above 1 × 10^4 Pa the R-t plot shows an expansion that corresponds to the drag model, given by the equation

$$R = R_0(1 - \exp(\beta t)) \tag{13}$$

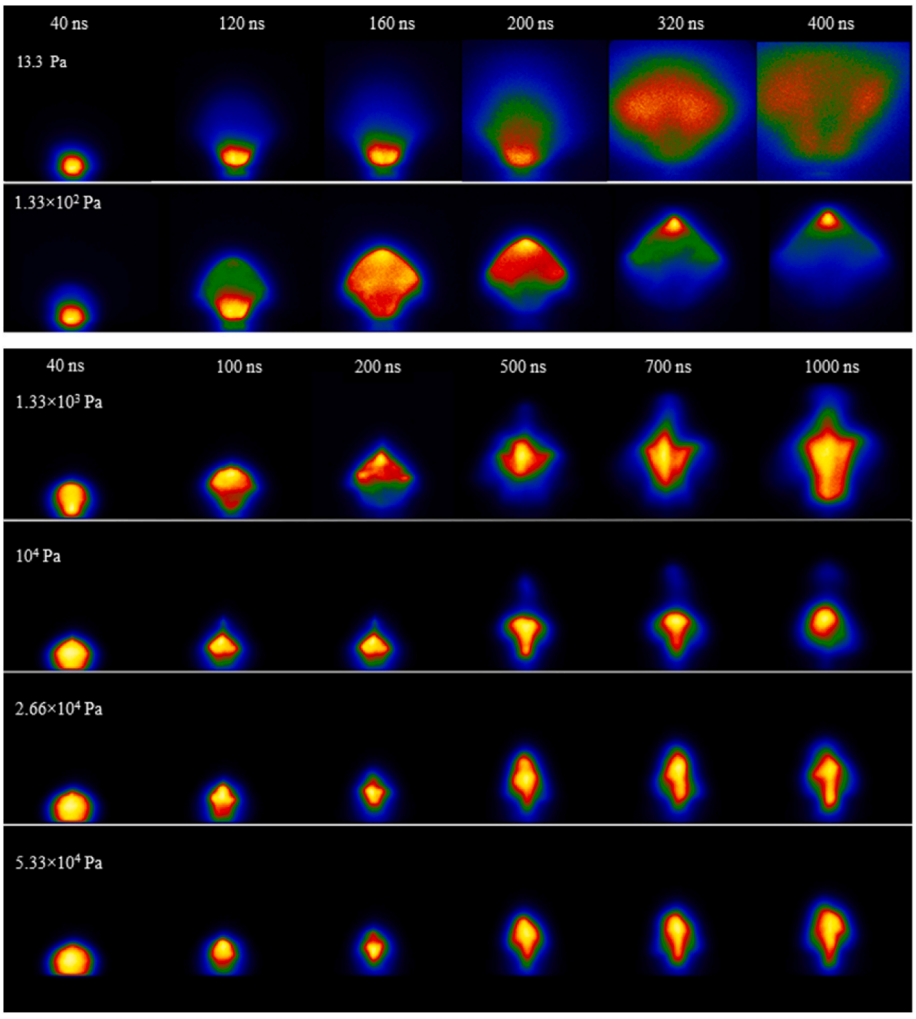

Fig. 11. Plume images at different ambient pressures and time delays. As seen from the electron density distribution, the emission from the plume changes from a spherical shape to an axially elongated shape after a few nanoseconds. The confinement effect can be seen for pressures higher than 1.33×10^2 Pa. Plume splitting at 1×10^4 Pa is also visible.

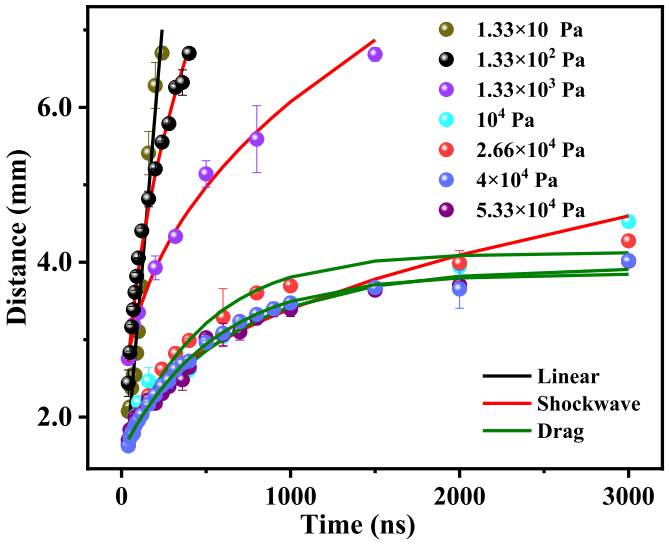

Fig. 12. R-t plots for different ambient pressures showing linear, shockwave and drag models fitted to plume front expansion.

Which predicts that the plume will eventually stop due to resistance from collisions with the background. Here R_0 represents the stopping distance, and β is the deceleration constant [29].

4. Conclusion

This study investigates the effect of intermediate ambient pressure (1.33×10^3 Pa - 5.33×10^4 Pa) on laser-produced tungsten plasma using optical emission spectroscopy (OES) and complementary plasma diagnostics methods. The Saha-Boltzmann method, Stark broadening of the Hα line, interferometry, and time-resolved plume imaging techniques are utilized to obtain the plasma parameters, radial electron density distribution, plume emission, and expansion dynamics. Number density calculations based on the Stark broadening of the Hα line and tungsten spectral line show a mutual strong correlation. An inhomogeneity in electron density distribution is observed within the pressure range studied. Despite its transient and inhomogeneous nature, the plasma is observed to be in local thermodynamic equilibrium (LTE) throughout the observation window. The transition from non-collective to collective behaviour of plasma is observed at the pressure of 1×10^4 Pa from shadowgraphy and time-resolved imaging. These findings provide valuable insights into the characteristics of laser-produced tungsten plasma at this pressure range, and can have significant implications for different fields of study, including materials science, and plasma fusion.

CRediT authorship contribution statement

M.S. Amogh: Writing – original draft, Methodology, Investigation, Conceptualization. **Sebin Sebastian Xavier:** Writing – original draft, Methodology, Investigation, Conceptualization. **Cyril Benny:** Writing – original draft, Investigation, Formal analysis. **Pranitha Sankar:** Methodology, Investigation. **Nancy Verma:** Methodology. **Reji Philip:** Writing – review & editing, Supervision, Resources, Project administration.

Declaration of competing interest

The authors declare that they have no known competing financial interests or personal relationships that could have appeared to influence the work reported in this paper.

Acknowledgment

Authors thank Dr. Sivanandan S. Harilal (PNNL, Richland, USA) for stimulating discussions.

Appendix A. Supplementary data

Supplementary data to this article can be found online at https://doi.org/10.1016/j.vacuum.2025.114449.

Data availability

Data will be made available on request.

References

[1] S. Zhang, et al., Laser-induced plasma temperature, Spectrochim. Acta Part B At. Spectrosc. 97 (Jul. 2014) 13–33, https://doi.org/10.1016/j.sab.2014.04.009.
[2] R.M. Ayub, et al., Langmuir probe characterization of spatially confined laser-induced Bismuth plasma, Optik 266 (Sep. 2022) 169566, https://doi.org/10.1016/j.ijleo.2022.169566.
[3] S.Q. Cao, et al., Dynamics and density distribution of laser-produced plasma using optical interferometry, Phys. Plasmas 25 (6) (Jun. 2018) 063302, https://doi.org/10.1063/1.5028414.
[4] J.S. Ross, et al., Thomson-scattering measurements in the collective and noncollective regimes in laser produced plasmas (invited), Rev. Sci. Instrum. 81 (10) (Oct. 2010) 10D523, https://doi.org/10.1063/1.3478975.
[5] C. Aragón, J.A. Aguilera, Characterization of laser induced plasmas by optical emission spectroscopy: a review of experiments and methods, Spectrochim. Acta Part B At. Spectrosc. 63 (9) (Sep. 2008) 893–916, https://doi.org/10.1016/j.sab.2008.05.010.
[6] F.J. Fortes, J. Moros, P. Lucena, L.M. Cabalín, J.J. Laserna, Laser-induced breakdown spectroscopy, Anal. Chem. 85 (2) (Jan. 2013) 640–669, https://doi.org/10.1021/ac303220r.
[7] J. Thomas, H. Chandra Joshi, Review on laser-induced breakdown spectroscopy: methodology and technical developments, Appl. Spectrosc. Rev. 59 (1) (Jan. 2024) 124–155, https://doi.org/10.1080/05704928.2023.2187817.
[8] J.L. Gottfried, Defense applications, in: Laser-Induced Breakdown Spectroscopy, Elsevier, 2020, pp. 275–310, https://doi.org/10.1016/B978-0-12-818829-3.00012-5.
[9] Laser-induced breakdown spectroscopy (LIBS) in cultural heritage, Anal. Methods 11 (45) (2019) 5833–5836, https://doi.org/10.1039/C9AY90147G.
[10] M.N. Khan, et al., A review on laser-induced breakdown spectroscopy in different cancers diagnosis and classification, Front. Physiol. 10 (Feb. 2022) 821057, https://doi.org/10.3389/fphy.2022.821057.
[11] R.C. Wiens, X. Wan, J. Lasue, S. Maurice, Laser-induced breakdown spectroscopy in planetary science, in: Laser-Induced Breakdown Spectroscopy, Elsevier, 2020, pp. 441–471, https://doi.org/10.1016/B978-0-12-818829-3.00020-4.
[12] S. Legnaioli, et al., Industrial applications of laser-induced breakdown spectroscopy: a review, Anal. Methods 12 (8) (2020) 1014–1029, https://doi.org/10.1039/C9AY02728A.
[13] S.S. Harilal, B.E. Brumfield, N.L. LaHaye, K.C. Hartig, M.C. Phillips, Optical spectroscopy of laser-produced plasmas for standoff isotopic analysis, Appl. Phys. Rev. 5 (2) (Jun. 2018) 021301, https://doi.org/10.1063/1.5016053.
[14] J. Hermann, C. Gerhard, E. Axente, C. Dutouquet, Comparative investigation of laser ablation plumes in air and argon by analysis of spectral line shapes: insights on calibration-free laser-induced breakdown spectroscopy, Spectrochim. Acta Part B At. Spectrosc. 100 (Oct. 2014) 189–196, https://doi.org/10.1016/j.sab.2014.08.014.
[15] G. Bertuccelli, H.O.D. Rocco, H.F. Ranea-Sandoval, Temperature and electron density gradient in Xe laser produced plasmas, by spectral analysis, J. Quant. Spectrosc. Radiat. Transf. 65 (4) (May 2000) 645–653, https://doi.org/10.1016/S0022-4073(99)00130-2.
[16] L. Mercadier, J. Hermann, C. Grisolia, A. Semerok, Diagnostics of nonuniform plasmas for elemental analysis via laser-induced breakdown spectroscopy: demonstration on carbon-based materials, J. Anal. At. Spectrom. 28 (9) (2013) 1446, https://doi.org/10.1039/c3ja50127b.
[17] S.S. Harilal, C.V. Bindhu, M.S. Tillack, F. Najmabadi, A.C. Gaeris, Plume splitting and sharpening in laser-produced aluminium plasma, J. Phys. Appl. Phys. 35 (22) (Nov. 2002) 2935–2938, https://doi.org/10.1088/0022-3727/35/22/307.
[18] J. Hermann, A. Lorusso, A. Perrone, F. Strafella, C. Dutouquet, B. Torralba, Simulation of emission spectra from nonuniform reactive laser-induced plasmas, Phys. Rev. E 92 (5) (Nov. 2015) 053103, https://doi.org/10.1103/PhysRevE.92.053103.
[19] S.M. Zaytsev, A.M. Popov, T.A. Labutin, Stationary model of laser-induced plasma: critical evaluation and applications, Spectrochim. Acta Part B At. Spectrosc. 158 (Aug. 2019) 105632, https://doi.org/10.1016/j.sab.2019.06.002.
[20] G. Cristoforetti, et al., Local thermodynamic equilibrium in laser-induced breakdown spectroscopy: beyond the McWhirter criterion, Spectrochim. Acta Part B At. Spectrosc. 65 (1) (Jan. 2010) 86–95, https://doi.org/10.1016/j.sab.2009.11.005.
[21] J. Liu, et al., Study of spectral intensity of the laser ablated tungsten plasma and ablation mass at various laser spot sizes and laser fluence in vacuum environment, Spectrochim. Acta Part B At. Spectrosc. 199 (Jan. 2023) 106569, https://doi.org/10.1016/j.sab.2022.106569.
[22] G.S. Maurya, A. Marín-Roldán, P. Veis, A.K. Pathak, P. Sen, A review of the LIBS analysis for the plasma-facing components diagnostics, J. Nucl. Mater. 541 (Dec. 2020) 152417, https://doi.org/10.1016/j.jnucmat.2020.152417.
[23] Z. He, et al., Quantitative characterization of helium in the ITER-like co-deposition layer by laser-induced breakdown spectroscopy, Nucl. Mater. Energy 36 (Sep. 2023) 101493, https://doi.org/10.1016/j.nme.2023.101493.
[24] K. Piip, et al., Loading of deuterium and helium by Pilot-PSI plasma and their detection by in-situ LIBS, Nucl. Mater. Energy 12 (Aug. 2017) 694–698, https://doi.org/10.1016/j.nme.2016.12.034.
[25] A. Talignani, et al., A review on additive manufacturing of refractory tungsten and tungsten alloys, Addit. Manuf. 58 (Oct. 2022) 103009, https://doi.org/10.1016/j.addma.2022.103009.
[26] V.N. Lednev, et al., In situ multi-elemental analysis by laser induced breakdown spectroscopy in additive manufacturing, Addit. Manuf. 25 (Jan. 2019) 64–70, https://doi.org/10.1016/j.addma.2018.10.043.
[27] M. Jiang, W. Tao, S. Wang, L. Li, Y. Chen, Effect of ambient pressure on interaction between laser radiation and plasma plume in fiber laser welding, Vacuum 138 (Apr. 2017) 70–79, https://doi.org/10.1016/j.vacuum.2017.01.012.
[28] X. Bai, et al., Quantitative analysis of tungsten in steel by one-point calibration laser-induced breakdown spectroscopy in vacuum, Spectrochim. Acta Part B At. Spectrosc. 206 (Aug. 2023) 106724, https://doi.org/10.1016/j.sab.2023.106724.
[29] H. Wu, et al., Spatiotemporal dynamic characterization of the laser-induced plasma of a mixed material (WCCu) under variable ablation angles in a vacuum, J. Anal. At. Spectrom. 37 (10) (2022) 2069–2081, https://doi.org/10.1039/D2JA00226D.
[30] D. Wu, et al., Temporal and spatial study of differently charged ions emitted by ns-laser-produced tungsten plasmas using time-of-flight mass spectroscopy, Plasma Sci. Technol. 23 (9) (Sep. 2021) 095505, https://doi.org/10.1088/2058-6272/ac08e1.
[31] H. Sattar, et al., Impact of microstructural properties on hardness of tungsten heavy alloy evaluated by stand-off LIBS after PSI plasma irradiation, J. Nucl. Mater. 540 (Nov. 2020) 152389, https://doi.org/10.1016/j.jnucmat.2020.152389.
[32] C. Fu, D. Wu, Q. Wang, L. Sun, Y. Wang, H. Ding, Time-resolved study of Bremsstrahlung emission and spectra at the early stage in a nanosecond laser ablated tungsten plasma, J. Instrum. 15 (2) (Feb. 2020), https://doi.org/10.1088/1748-0221/15/02/C02022. C02022–C02022.
[33] D. Zhao, et al., Highly depth-resolved characterization of fusion-related tungsten material based on picosecond laser-induced breakdown spectroscopy, J. Anal. At. Spectrom. 35 (12) (2020) 2867–2879, https://doi.org/10.1039/D0JA00340A.
[34] D. Wu, et al., Parameter optimization of the spectral emission of laser-induced tungsten plasma for tokamak wall diagnosis at different pressures, J. Anal. At. Spectrom. 36 (6) (2021) 1159–1169, https://doi.org/10.1039/D1JA00009H.
[35] E. Mal, R. Junjuri, M.K. Gundawar, A. Khare, Temporal characterization of laser-induced plasma of tungsten in air, Laser Part. Beams 38 (1) (Mar. 2020) 14–24, https://doi.org/10.1017/S0263034619000788.
[36] W.M. Steen, Principles of optics M. Born and E. Wolf, 7th (expanded) edition, cambridge university press, cambridge, 1999, 952pp. 37.50/US $59.95, ISBN 0-521-64222-1, Opt Laser. Technol. 32 (5) (Jul. 2000) 385, https://doi.org/10.1016/S0030-3992(00)00061-X.
[37] S.S. Harilal, M.C. Phillips, D.H. Froula, K.K. Anoop, R.C. Issac, F.N. Beg, Optical diagnostics of laser-produced plasmas, Rev. Mod. Phys. 94 (3) (Aug. 2022) 035002, https://doi.org/10.1103/RevModPhys.94.035002.
[38] D. Nishijima, R.P. Doerner, Stark width measurements and Boltzmann plots of W I in nanosecond laser-induced plasmas, J. Phys. Appl. Phys. 48 (32) (Aug. 2015) 325201, https://doi.org/10.1088/0022-3727/48/32/325201.
[39] D. Dojić, N.V. Nedić, S. Bukvić, Stark width parameter measurements of singly ionized tungsten spectral lines in laser-induced plasma, Spectrochim. Acta Part B At. Spectrosc. 209 (Nov. 2023) 106795, https://doi.org/10.1016/j.sab.2023.106795.

[40] J. Ashkenazy, R. Kipper, M. Caner, Spectroscopic measurements of electron density of capillary plasma based on Stark broadening of hydrogen lines, Phys. Rev. A 43 (10) (May 1991) 5568–5574, https://doi.org/10.1103/PhysRevA.43.5568.
[41] Z. Mijatović, et al., Plasma density determination by using hydrogen Balmer Hα spectral line with improved accuracy, Spectrochim. Acta Part B At. Spectrosc. 166 (Apr. 2020) 105821, https://doi.org/10.1016/j.sab.2020.105821.
[42] A.M. El Sherbini, H. Hegazy, Th M. El Sherbini, Measurement of electron density utilizing the Hα-line from laser produced plasma in air, Spectrochim. Acta Part B At. Spectrosc. 61 (5) (May 2006) 532–539, https://doi.org/10.1016/j.sab.2006.03.014.
[43] P. Kepple, H.R. Griem, Improved Stark profile calculations for the hydrogen lines H α , H β , H γ , and H δ, Phys. Rev. 173 (1) (Sep. 1968) 317–325, https://doi.org/10.1103/PhysRev.173.317.
[44] A.V. Bulgakov, N.M. Bulgakova, Dynamics of laser-induced plume expansion into an ambient gas during film deposition, J. Phys. Appl. Phys. 28 (8) (Aug. 1995) 1710–1718, https://doi.org/10.1088/0022-3727/28/8/022.
[45] P.T. Rumsby, J.W.M. Paul, Temperature and density of an expanding laser produced plasma, Plasma Phys. 16 (3) (Mar. 1974) 247–260, https://doi.org/10.1088/0032-1028/16/3/002.
[46] A. Sarkar, M. Singh, Laser-induced plasma electron number density: Stark broadening method versus the Saha–Boltzmann equation, Plasma Sci. Technol. 19 (2) (Feb. 2017) 025403, https://doi.org/10.1088/2058-6272/19/2/025403.
[47] J.A. Aguilera, C. Aragón, Characterization of a laser-induced plasma by spatially resolved spectroscopy of neutral atom and ion emissions, Spectrochim. Acta Part B At. Spectrosc. 59 (12) (Dec. 2004) 1861–1876, https://doi.org/10.1016/j.sab.2004.08.003.
[48] A.K. Shaik, M.P. Polek, E.J. Kautz, A.M. Casella, D.J. Senor, S.S. Harilal, The influence of laser energy on deuterium emission characteristics from a Zircaloy-4 plasma, Phys. Plasmas 31 (10) (Oct. 2024) 103505, https://doi.org/10.1063/5.0220128.
[49] A.V.F. Zuffi, J. Ricardo Dos Santos, E.P. Maldonado, N.D. Vieira, R.E. Samad, Femtosecond laser-plasma dynamics study by a time-resolved Mach–Zehnder-like interferometer, Appl. Opt. 62 (8) (Mar. 2023) C128, https://doi.org/10.1364/AO.477395.
[50] J. Park, H.A. Baldis, H. Chen, The implementation and data analysis of an interferometer for intense short pulse laser experiments, High Power Laser Sci. Eng. 4 (2016) e26, https://doi.org/10.1017/hpl.2016.21.
[51] M. Polek, F. Beg, S. Harilal, The role of laser wavelength on the early-stage electron density evolution in laser-produced plasma, in: C.R. Phipps, V.E. Gruzdev (Eds.), High-Power Laser Ablation VIII, SPIE, Santa Fe, United States, Apr. 2024, p. 87, https://doi.org/10.1117/12.3016463.
[52] P. Hough, C. McLoughlin, T.J. Kelly, S.S. Harilal, J.P. Mosnier, J.T. Costello, Time resolved Nomarski interferometery of laser produced plasma plumes, Appl. Surf. Sci. 255 (10) (Mar. 2009) 5167–5171, https://doi.org/10.1016/j.apsusc.2008.08.050.
[53] C.J. Dasch, One-dimensional tomography: a comparison of Abel, onion-peeling, and filtered backprojection methods, Appl. Opt. 31 (8) (Mar. 1992) 1146, https://doi.org/10.1364/AO.31.001146.
[54] A. De Giacomo, M. Dell'Aglio, R. Gaudiuso, S. Amoruso, O. De Pascale, Effects of the background environment on formation, evolution and emission spectra of laser-induced plasmas, Spectrochim. Acta Part B At. Spectrosc. 78 (Dec. 2012) 1–19, https://doi.org/10.1016/j.sab.2012.10.003.
[55] R.K. Singh, J. Narayan, Pulsed-laser evaporation technique for deposition of thin films: physics and theoretical model, Phys. Rev. B 41 (13) (May 1990) 8843–8859, https://doi.org/10.1103/PhysRevB.41.8843.
[56] J. Nilsen, W.R. Johnson, C.A. Iglesias, J.H. Scofield, Impact of anomalous dispersion on the interferometer measurements of plasmas, J. Quant. Spectrosc. Radiat. Transf. 99 (1–3) (May 2006) 425–438, https://doi.org/10.1016/j.jqsrt.2005.05.034.
[57] J. Filevich, et al., Observation of a multiply ionized plasma with index of refraction greater than one, Phys. Rev. Lett. 94 (3) (Jan. 2005) 035005, https://doi.org/10.1103/PhysRevLett.94.035005.
[58] J. Nilsen, W.R. Johnson, Plasma interferometry and how the bound-electron contribution can bend fringes in unexpected ways, Appl. Opt. 44 (34) (Dec. 2005) 7295, https://doi.org/10.1364/AO.44.007295.
[59] J. Filevich, et al., Prediction and observation of tin and silver plasmas with index of refraction greater than one in the soft x-ray range, Phys. Rev. E 74 (1) (Jul. 2006) 016404, https://doi.org/10.1103/PhysRevE.74.016404.
[60] G. O'Sullivan, et al., Emission and absorption in laser produced plasmas: processes and applications, J. Phys. Conf. Ser. 163 (Apr. 2009) 012003, https://doi.org/10.1088/1742-6596/163/1/012003.
[61] J. Buday, P. Pořízka, M. Buchtová, J. Kaiser, Determination of initial expansion energy with shadowgraphy in laser-induced breakdown spectroscopy, Spectrochim. Acta Part B At. Spectrosc. 182 (Aug. 2021) 106254, https://doi.org/10.1016/j.sab.2021.106254.
[62] X. Bai, F. Cao, V. Motto-Ros, Q. Ma, Y. Chen, J. Yu, Morphology and characteristics of laser-induced aluminum plasma in argon and in air: a comparative study, Spectrochim. Acta Part B At. Spectrosc. 113 (Nov. 2015) 158–166, https://doi.org/10.1016/j.sab.2015.09.023.
[63] M. Gatti, V. Palleschi, A. Salvetti, D.P. Singh, M. Vaselli, Spherical shock waves in laser produced plasmas in gas, Opt. Commun. 69 (2) (Dec. 1988) 141–146, https://doi.org/10.1016/0030-4018(88)90299-4.
[64] M. Hendijanifard, D.A. Willis, Validity of the taylor-sedov theory for studying laser-induced phase explosion and shock waves, J. Nanosci. Nanotechnol. 15 (4) (Apr. 2015) 3249–3253, https://doi.org/10.1166/jnn.2015.9649.
[65] E.H. Kwapis, M. Hewitt, K.C. Hartig, Shock physics and shadowgraphic measurements of laser-produced cerium plasmas, Opt. Express 31 (6) (Mar. 2023) 10694, https://doi.org/10.1364/OE.483055.